PAPER • **OPEN ACCESS**

Effects of two wet exfoliation strategies on the yield and colloidal behavior of 2D hexagonal boron nitride nanosheets

To cite this article: Anika Azme *et al* 2025 *Nano Ex.* **6** 015011

NANO EXPRESS

PAPER

Effects of two wet exfoliation strategies on the yield and colloidal behavior of 2D hexagonal boron nitride nanosheets

Anika Azme[1], **Isabel C Escobar**[2], **Olga Tsyusko**[3] **and Nirupam Aich**[1]

[1] Department of Civil and Environmental Engineering, University of Nebraska - Lincoln, Lincoln, NE, 68588, United States of America
[2] Department of Chemical and Materials Engineering, University of Kentucky, Lexington, KY, 40506, United States of America
[3] Department of Plant and Soil Sciences, University of Kentucky, Lexington, KY, 40546, United States of America

E-mail: nirupam.aich@unl.edu

Keywords: hexagonal boron nitride, 2D nanomaterials, Exfoliation, colloidal stability, Sonication

Supplementary material for this article is available online

OPEN ACCESS

RECEIVED
29 October 2024

REVISED
25 December 2024

ACCEPTED FOR PUBLICATION
22 January 2025

PUBLISHED
19 February 2025

Abstract

We report the exfoliation process optimization, physicochemical characterizations, and comparative aggregation behavior of the inorganic 2D nanomaterial hexagonal Boron Nitride (h-BN) produced from two repetitive sonication-centrifugation processes with varying centrifugation speeds and recycle frequency: Continuous and Segmented protocols. Enhancing exfoliation efficiency and understanding aqueous stability are essential for sustainable design and environmental applications. Results showed that the Segmented protocol outperformed the Continuous protocol by having a six-fold increase in the exfoliated h-BN nanosheet yield by reusing the unexfoliated bulk h-BN and decreasing centrifugation speeds. Centrifugation speeds of 1880 and 950 rpm produced nanosheets of similar sizes due to the slight difference in the centrifugal force generated in both protocols. Moreover, nanosheets from both protocols had enhanced polarity due to the higher amounts of −OH bonds attached to the exposed edges of the nanosheets. However, the hydroxylation percentage of the nanosheets decreased with centrifugation speed. Both protocols produced h-BN nanosheets that were stable in DI water dispersion. The comparatively lower initial aggregation rate at all centrifugation speeds supported the fact that the Segmented protocol nanosheets were more stable than the Continuous ones. The Segmented protocol h-BN nanosheets showed better overall stability at lower speeds than the other centrifugation speeds. Segmented protocol nanosheets from 3750 rpm had the lowest aggregation rate than the other centrifugation speed. These findings assist in finding the balance between exfoliation protocol, environmental application, and implication of h-BN nanosheets.

1. Introduction

Two-dimensional (2D) nanomaterials are receiving increasing attention due to their ultrathin structure and promising features. Graphene-analogous hexagonal boron nitride (h-BN) is a sp^2 hybridized network of the same amounts of boron (B) and nitrogen (N) organized in a honeycomb structure [1]. Their wide bandgap [2], high thermal conductivity [3], electron tunneling property [4], mechanical strength [5], biocompatibility [6], and photoluminescence [7] make them suitable for applications in photodetectors [8], bioimaging, drug delivery, and biosensing [9]. Their usage has recently been expanded for water remediation through contaminant adsorption and degradation. This nanomaterial has excellent performance as an adsorbent to remove organic [10, 11] and inorganic pollutants [10, 12]. They have also been used independently or as cocatalysts to degrade organic contaminants via photocatalytic activity [2, 13–17]. This increasing usage potential indicates the need for sustainable and scalable production of high-quality 2D h-BN nanosheets [18].

2D h-BN nanosheets are obtained using bottom-up methods like chemical vapor deposition, pulsed layer deposition, thermal plasma, and pyrolysis, and top-down methods like mechanical cleavage, laser ablation, chemical weathering, and liquid phase exfoliation [19–21]. Among these, liquid phase exfoliation is one of the

most investigated methods for exfoliating 2D nanomaterials in a scalable manner [1]. This method uses sonication in a liquid media dispersion of bulk h-BN to exfoliate individual layers and centrifugation to separate the exfoliated portion of the dispersion from the unexfoliated counterpart. Different solvents including N-methylpyrrolidone (NMP) [22], isopropanol [23], ionic liquids [24], N, N-dimethylformamide (DMF) [25], and water [26] have been explored to produce 2D h-BN nanosheets. Most of these procedures use high-energy sonication for an extended period (8–96 h) [22–26], high-temperature pretreatment (180 °C–1000 °C) [27, 28], and high-speed centrifugation (4000–10000 rpm) [1, 22, 25] to obtain the exfoliated nanosheets. Despite the considerable effort required for these processes, the reported yield and concentrations of exfoliated h-BN nanosheets are low (0.04–6.8%) [22–26]. This overall low yield could be attributed to the partial ionic nature of the interlayer bonding present in these 2D nanosheets [29, 30]. Some processes are able to achieve comparatively high yields (>10%) through complicated procedures such as adding chemical agents—metal [1], gelatin [31], and salts [22, 24] during sonication.

By improving the yield of the h-BN nanosheets, bulk h-BN waste might be minimized. One approach to reducing material wastage is reusing the unexfoliated bulk materials for repetitive rounds of sonication and centrifugation. It has been reported that one additional cycle of brief sonication and centrifugation might increase total exfoliation yield [24]. Another work used isopropyl alcohol (IPA): water solvent to increase the yield through this process [32]. While these protocols provide higher yields of nanosheets, the solvents used here have shown moderate toxicity levels [33, 34]. For sustainable application, less hazardous and simple solvents, such as ethanol: water solutions, might be used for increasing the exfoliation efficiency via sonication. The previous studies have shown that ethanol: water solution is an effective medium for exfoliating h-BN nanosheets via sonication [35–38]. A successful exfoliating solvent should have surface tension close to that of h-BN (35 mN m^{-1}) to reduce the exfoliation energy, maximize dispersion efficiency, and inhibit reaggregation [39–41]. Mixing ethanol and water creates a solvent with a surface tension of 30.69 mN m^{-1}, higher than pure ethanol (22.31 mN m^{-1}) and lower than pure water (72.75 mN m^{-1}) at 20 °C [42]. As this is the recommended range (30–40 mN m^{-1}) for successful exfoliation, this mixed solvent provides a better exfoliation yield than the pure ones [38]. Along with this, the ethanol-water solvent is low-cost and less toxic. The lower viscosity of the mixed solvent also reduces the solution's resistance to the ultrasonic probe's movement, leading to increased cavitation and efficient exfoliation [43, 44]. For these reasons, the ethanol-water solvent needs to be used for the repetitive sonication centrifugation process to increase the exfoliation yield of h-BN nanosheets. Moreover, subsequent centrifugation at different speeds would efficiently separate h-BN nanosheets with varying sizes and thickness ranges from the unexfoliated materials [23, 45, 46]. Variable centrifugation speed during wet exfoliation processes via sonication-centrifugation might be utilized to optimize the exfoliation process and reduce material wastage. Therefore, the repetitive sonication centrifugation processes using ethanol: water solvent and varying centrifugation speed need to be investigated to evaluate changes in h-BN nanosheet yield. However, no such studies exist in the literature.

Furthermore, given the increasing consideration of exfoliated h-BN nanosheets for applications in environmental remediation, it is vital to prioritize a comprehensive understanding of its behavior in aqueous media [35, 47, 48]. The colloidal stability of h-BN in aquatic environments is a critical factor influencing their bioavailability and interactions with environmental organisms [49, 50]. This knowledge will also assist in the practical design and implementation of environmental applications that involve the aqueous dispersion of similar 2D nanomaterials [51–54]. Sonication of bulk h-BN in the presence of different solvents exfoliates and induces different extents of changes in the physicochemical properties of the resulting exfoliated h-BN nanosheets. Based on the exfoliant solvent, different functional groups attach to the h-BN nanosheets' surface and significantly alter the nanosheets' chemical properties. With water in the exfoliant solvent, hydroxyl (−OH) groups attached to the nanosheets during sonication and increase the polarity of the h-BN nanosheets [24, 26, 55]. Based on the enhanced polarity of these h-BN nanosheets, their aqueous dispersibility might change. As varying centrifugation speeds separate exfoliated h-BN nanosheets of different lateral sizes and layer thickness ranges, their subsequent differences in physicochemical properties potentially influence the nanosheets' aggregation behavior in aqueous media. Previous research on the aggregation behavior of 2D h-BN nanosheet and 3D h-BN nanosphere focused on ion effects [35, 56] and the presence of other stabilizing agents [57] rather than the exfoliation process of these nanomaterials. The focus of this study was to address the knowledge gap in understanding the influence of the exfoliation processes on the colloidal stability of h-BN nanosheets. Gaining insight into this aspect might help optimize their exfoliation process and usage for water remediation purposes.

The objectives of this paper were to (i) compare the yield of h-BN nanosheets from two repetitive sonication-centrifugation processes, (ii) examine the changes in physical morphology, chemical structures, and electrokinetic properties of the exfoliated nanosheets obtained from these two processes, and (iii) evaluate the effects of the exfoliation process on the colloidal behavior of the exfoliated h-BN nanosheets in the aquatic environment using DI water and an EPA standard toxicity testing media, Moderately Hard Reconstituted Water

(MHRW) [58]. A non-hazardous solvent, ethanol: water solution, was used to exfoliate the h-BN nanosheets. In one exfoliation method, the precipitated unexfoliated h-BN from the initial exfoliation cycle was reused for eight sonication cycles, with the centrifugation speed being reduced every three cycles. This approach allows the nanosheets obtained to reflect the combined effects of both sonication time and centrifugation speed. In the second method, bulk h-BN was reused for three sonication cycles only for a specific centrifugation speed. This method focuses on the influence of centrifugation speed, producing nanosheets that primarily demonstrate speed effects without additional contributions from extended sonication. In both protocols, centrifugation speeds of 3750, 1880, and 950 rpm were used to obtain h-BN nanosheets of varying size ranges. For determining the physicochemical properties of the nanosheets, High Resolution Transmission Electron Microscopy (HRTEM), Scanning Transmission Electron Microscopy (STEM), Energy Dispersive X-ray Spectroscopy (EDS), and X-ray Photoelectron Spectroscopy (XPS) were employed. For measuring the effect of different exfoliation processes and centrifugation speeds on the colloidal stability of the nanosheets, hydrodynamic diameter, surface charge, and initial aggregation rate of the h-BN nanosheets dispersed in DI water were measured using a Zetasizer and time-resolved dynamic light scattering (TRDLS) technique. The effect of ionic strength on the colloidal stability of the exfoliated nanosheets from different protocols was also studied by dispersing them in DI and MHRW to elucidate their environmental application potential. The EPA standard toxicity media MHRW was used to determine the h-BN nanosheets' potential for environmental implications.

2. Experimental section

2.1. Materials

Boron Nitride Ultrafine Powder (99%) or bulk hexagonal Boron Nitride was purchased from Graphene Supermarket, Ronkonkoma, NY. Ethanol (Anhydrous, 200 proof) was obtained from the Decon Labs, Inc. King of Prussia, PA. The salts Potassium Chloride (99+%, ACS, Fisher Scientific), Sodium Bicarbonate (99+%, ACS, Fisher Scientific), Magnesium Sulfate Heptahydrate (98+%, ACS, Sigma Aldrich), and Calcium sulfate dihydrate (98+%, ACS, Sigma Aldrich) were used to prepare the Moderately Hard Reconstituted Water (MHRW) [58].

2.2. Methods

2.2.1. h-BN nanosheet exfoliation process

For both protocols, 1 g bulk h-BN was placed in a 500 mL glass beaker. 90 mL Ethanol was added to the beaker, followed by 110 mL Deionized (DI) water to create a 200 mL 45:55 Ethanol: DI water dispersion. The dispersion was sonicated for 3 h using a probe sonicator Q700 (Qsonica, Newtown, CT) with a 1/4″ (6.4 mm) microtip probe (#4420). The amplitude of the sonicator was set to 50 corresponding to a power input of 22–25 W. The pulse on and off times were set as 8 s and 2 s, respectively. After sonication, the solution was transferred to 50 mL polypropylene conical tubes and centrifuged at 3750 rpm to separate the supernatant with Centrifuge Sorvall Legend RT (Thermo Fisher Scientific, USA). The precipitate from the first batch was returned to the sonicator after adding 90 mL ethanol and 110 mL DI water successively. The supernatant was decanted in a 200 mL glass beaker and kept in the oven (Shel Lab Economy Vacuum Oven, SVAC2E, Sheldon Manufacturing, GA) at 85 °C. The dried h-BN powder was scraped with a stainless-steel laboratory spatula with a scoop and stored in a 20 mL aluminum foil-wrapped scintillation vial at 20 °C until further use.

For the first protocol of repetitive sonication-centrifugation, this cycle was repeated 8 times with the centrifuge speed reducing every three cycles. The centrifuge speed was varied to separate h-BN nanosheets with wider particle size distributions. The first three batches were centrifuged at 3750 rpm, the next three at 1880 rpm, and the last at 950 rpm. This exfoliation sequence is denoted as the Continuous protocol, and the h-BN nanosheets obtained from 3750, 1880, and 950 rpm are addressed as C3750, C1880, and C950, respectively. For the second exfoliation sequence, the exfoliated h-BN nanosheets were produced in a similar repetitive sonication centrifugation cycle, with only new bulk h-BN being introduced for every three cycles of different centrifugation speeds. This sequence is further denoted as the Segmented protocol, and the h-BN nanosheets obtained from 3750, 1880, and 950 rpm are addressed as S3750, S1880, and S950, respectively. Figure 1 shows the general scheme of the repetitive sonication-centrifugation procedure for h-BN nanosheet exfoliation. Table 1 lists the total sonication time, centrifugation speed for both protocols, and the amount of bulk h-BN used.

2.2.2. h-BN nanosheet characterization

The physicochemical properties of the exfoliated h-BN nanosheets were characterized using HRTEM, STEM, EDS, and XPS. The second sub-batch from each centrifugation speed (B, E, and H) was used for both protocols for these characterizations (Except for C3750, sub-batch A, B, and C were mixed). For HRTEM, STEM, and EDS

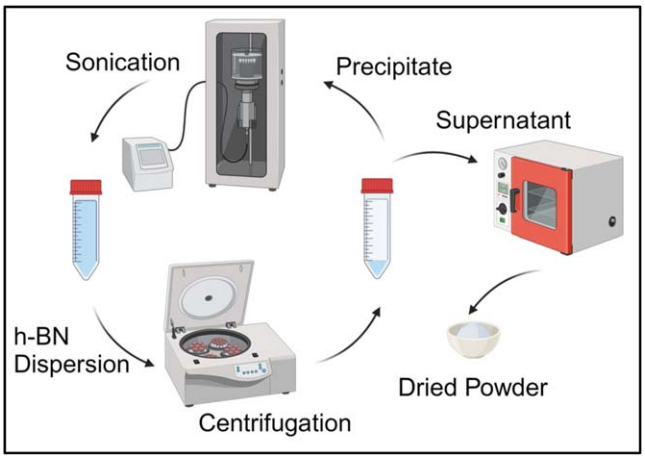

Figure 1. Schematic illustration of h-BN nanosheet exfoliation protocol.

Table 1. Sonication time and centrifugation speed for different h-BN nanosheets.

Sub-batch	Bulk h-BN mass (gram)		Total sonication time (hours)		Centrifugation speed (rpm)
	Continuous	Segmented	Continuous	Segmented	
A			3	3	3750
B		1 (reused for A-C)	6	6	3750
C			9	9	3750
D			12	3	1880
E	1 (reused for A-I)	1 (reused for D-F)	15	6	1880
F			18	9	1880
G			21	3	950
H		1 (reused for G-I)	24	6	950
I			27	9	950

images, the h-BN powder was placed in a 10 ml glass beaker, followed by ethanol, to prepare a homogeneous 0.1 mg ml^{-1} dispersion. The dispersion was bath sonicated for 5 min using the Emerson Branson M3800 Bath Sonicator (St. Louis, MO). Then, 5 μl of this dispersion was dropped 3–4 times on carbon-coated copper TEM grids (200 mesh, TedPella Inc., Redding, CA). A kimwipe was used to remove the excess ethanol from the grid bottom after each drop for faster drying and lesser aggregation of the nanosheets. The grid was then placed on an aluminum foil wrapped hotplate surface at 60 °C until the drying was complete, and then the dried nanosheet containing TEM grid was transferred to the sample holder for the HRTEM. The HRTEM images of the h-BN nanosheets were captured using FEI Tecnai Osiris (Scanning) Transmission Electron Microscope (STEM) with an accelerating voltage of 200 kV and equipped with Electron Dispersive Spectroscopy (EDS), placed at the Nebraska Center for Materials and Nanoscience (NCMN) at the University of Nebraska- Lincoln (UNL). For each condition (speed and protocol), 30 individual nanosheets from the STEM images were analyzed using ImageJ software (National Institutes of Health, USA) to estimate the lateral dimension distribution of the h-BN nanosheets [59–61]. According to the Central Limit Theorem (CLT), the mean would be a normal distribution of a sample with $\geqslant$30 size, irrespective of the actual population distribution. This normal distribution of the sample mean enabled statistical technique applications such as confidence intervals and hypothesis testing. Using a sample size of 30 also reduced the standard deviation of mean (SDM), ensuring the confidence interval (CI) was reasonably narrow and precise. The Fast Fourier Transform (FFT) and inverse FFT images were analyzed to determine the layer-to-layer distance, atomic distance, and angular measurements of the h-BN nanosheets using the ImageJ software. The high-angle annular dark field (HAADF) images of the bulk and exfoliated h-BN nanosheets were captured using the STEM imaging mode. The EDS tool acquired the intensity spectrum generated from the part of the bulk and exfoliated h-BN captured in the HAADF-STEM images as a function of x-ray energy (up to 20 keV). Elements were selected for elemental mapping of the bulk and exfoliated h-BN nanosheets based on the peaks from these intensity graphs.

The atomic composition and bonding characteristics of the exfoliated h-BN nanosheets were analyzed using XPS valence band spectra with the Thermo Scientific K-alpha+ Surface Analysis XPS/UPS System (Thermo

Fisher Scientific Inc., Waltham, MA). The dried h-BN nanosheet powder was placed on a double-sided copper tape, ensuring a consistent depth of the powder across the tape before degassing inside a chamber overnight. XPS spectra were acquired by irradiating a solid surface of exfoliated h-BN nanosheet powder with Al Kα x-rays at 1486.6 eV. Concurrently, the kinetic energy of photoelectrons emitted from the top 1–10 nm of the analyzed material was measured. The XPS data was analyzed for peak fitting using the CasaXPS software version 2.3.25PR1.0.

2.2.3. Preparation of moderately hard reconstituted water (MHRW)

The MHRW was prepared following the EPA protocol [58]. 500 mL DI water was added to a 500 mL volumetric flask. Then, salts were added in this order: 61.25 mg of $MgSO_4.7H_2O$, 48 mg of $NaHCO_3$, 30 mg of $CaSO_4.2H_2O$, and 2.0 mg of KCl. The flask was shaken well to dissolve the added salt before moving to the next one. The pH of the solution ~7.8–8.0 was measured after storing for 24 h. The ionic strength of the final MHRW solution was calculated to be 5.16 mM. The solution was stored at 4 °C for later use.

2.2.4. Surface charge and colloidal stability analysis

The surface charge and colloidal stability of the exfoliated nanosheets were measured using the electrophoresis and TRDLS techniques, respectively [35, 62]. The Malvern ZetaSizer Nano ZS90 equipped with a 4 mW He−Ne 633 nm laser (Malvern Instrument, Worcestershire, UK) was used to measure the zeta potential and hydrodynamic diameter. The dried h-BN nanosheet powder was homogeneously dispersed by sonicating it for more than 5 min with a bath sonicator in different aqueous media (DI and MHRW) to form a 0.1 mg mL^{-1} suspension. The zeta potential was measured by placing 800 μL h-BN nanosheet dispersion in the disposable Malvern Panalytical folded capillary zeta cell. At least 10 zeta potential measurements were recorded for each h-BN nanosheet sample. Around 1.2 mL of the 0.1 mg mL^{-1} h-BN suspension was transferred to a four clear-sided disposable polystyrene square cuvette and placed inside the ZetaSizer chamber for size measurement. The hydrodynamic diameter measurement was obtained continuously for 30 min with 15 s intervals between data collection using the 90° scattering detector angle [35]. The refractive index and absorption coefficient for h-BN nanosheets were 2.2 and 0.01, respectively [35, 63]. This measurement is the projected size of a sphere that can scatter light similarly to the particle that is being measured. The DLS technique employed by the Zetasizer instrument measured the scattering intensity of particles moving due to Brownian motion and calculated the Z-Avg value using the Stokes–Einstein equation. After collecting the hydrodynamic diameter information, the Zetasizer software used algorithms to calculate the decay rate of the correlation function to produce particle size distribution. This was used as an approximated size estimation to compare the hydrodynamic diameters of the bulk and exfoliated nanosheets from two different protocols [35, 64, 65]. The intensity averaged Z-Avg value can provide a highly useful understanding of the nanosheet size distribution in the dispersion [66]. The results for these nanosheet samples are still comparable as they have been measured using the same dispersant and technique following the instrument guideline.

2.2.5. Statistical analysis

The OriginPro 2024 software was used to perform the statistical analysis for this study. The Two-way Analysis of Variance (ANOVA) method was used to determine the overall statistical significance of the influence of exfoliation parameters on the lateral area distribution of the h-BN nanosheets. The three-way ANOVA method was used to determine the statistical significance of the influence of exfoliation parameters and dispersion media on the surface charge and colloidal stability of the exfoliated h-BN nanosheets. For the ANOVA analysis, the probability level with $p < 0.05$ was considered statistically significant. The above ANOVA analysis cases also included Post hoc Tukey's test to identify which groups' means differ. Group means are considered significantly different when classified with different letters.

3. Results and discussion

3.1. Physicochemical property characterization

3.1.1. Physical morphology

Figure 2 provides information on the h-BN nanosheet yield and physical morphology changes in the bulk and exfoliated h-BN nanosheets from the two exfoliation protocols used in this study, Continuous and Segmented, using high magnification TEM images (5–20 nm). Figure 2(a) compares the exfoliation yield between these two protocols. The overall yield increased 3–6 folds by reusing the unexfoliated h-BN. By reusing the bulk h-BN, the total yield increased from 1.33 (for single-time sonication) to 5.85% at the centrifugation speed of 3750 rpm, 2.24 to 7.02% at 1880 rpm, and 3.96 to 11% at 950 rpm for the Continuous exfoliation protocol. For the Segmented exfoliation protocol, the total yield increased from 1.56% to 5.99%, 2.70% to 11.03%, and 3.54% to

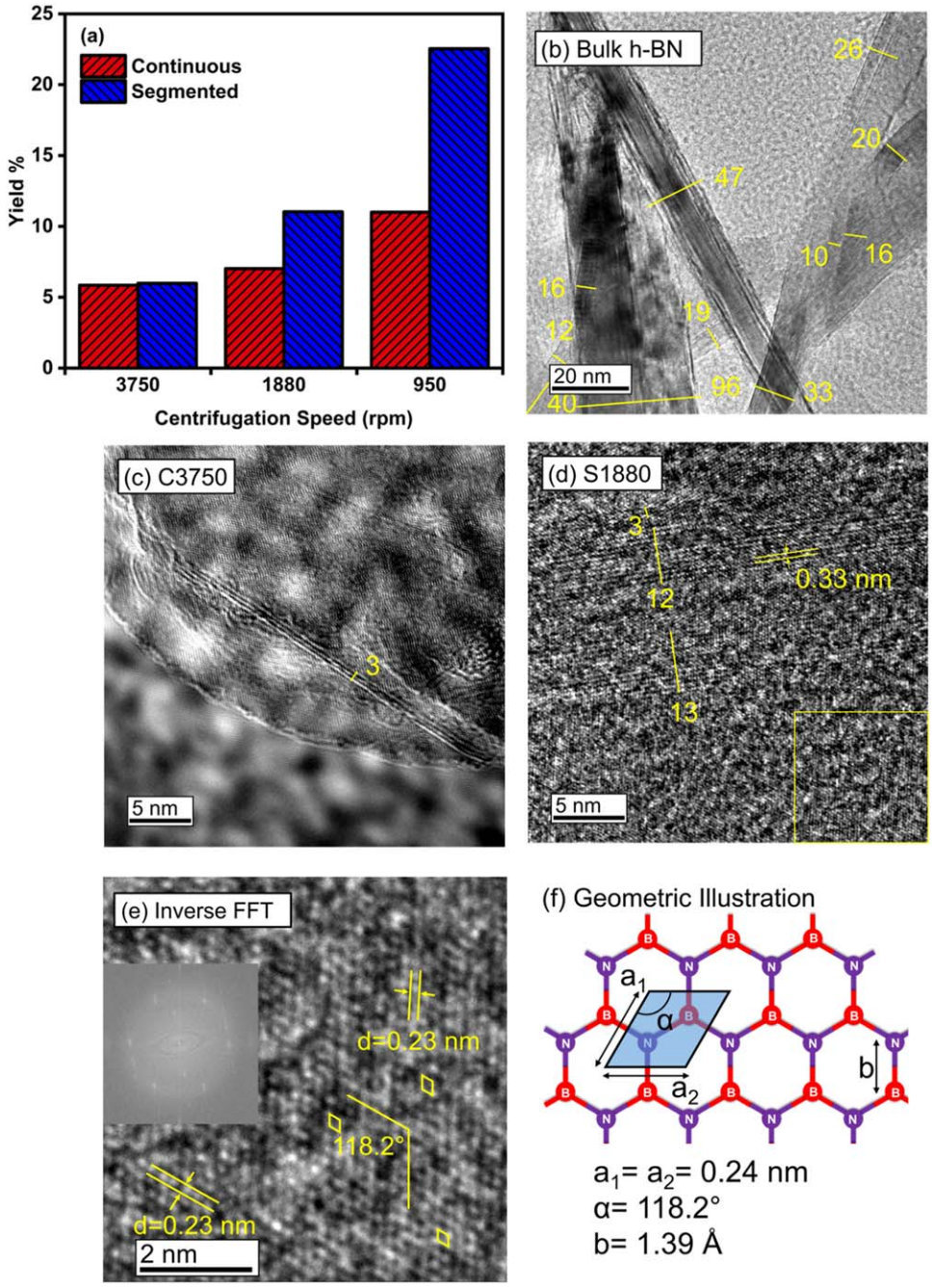

Figure 2. (a) Yield comparison of Continuous and Segmented protocols under varying centrifugation speeds showcasing higher yield of h-BN nanosheets from Segmented protocol and low centrifugation speed of 950 rpm, HRTEM images of (b) bulk h-BN documenting 10–96 layers of h-BN nanosheets, (c) h-BN nanosheets with 3 layers from Continuous protocol, and (d) h-BN nanosheets with 3–13 layers from Segmented protocol, (e) inverse FFT image of figure 2(d) with rhombus-shaped unit cells labeled for hexagonal lattice and corresponding FFT as inset, and (f) representative illustration of the basal plane of a single layer of h-BN nanosheet with the two atom-based rhombus-shaped unit cell and the associated geometrics.

22.53% for centrifugation speeds 3750, 1880, and 950 rpm, respectively. This indicates unexfoliated h-BN from the precipitate are able to produce more h-BN nanosheets via repeated cycles of sonication and centrifugation. This, in turn, increases the total yield of h-BN nanosheets. With a decrease in centrifugation speed from 3750 to 950 rpm, the h-BN nanosheet yield increased as lesser h-BN nanosheets were precipitated at a lower speed. Using new bulk h-BN for different centrifugation speeds in the Segmented protocol yielded a higher amount of h-BN nanosheets compared to the Continuous one. While a higher centrifugation speed of 3750 rpm produced a similar yield of h-BN nanosheets for both protocols, the lower centrifugation speeds at 1880 and 950 rpm provided higher h-BN nanosheet yields in the Segmented protocol compared to the Continuous one. In the Continuous protocol, the initial h-BN mass used for the exfoliation decreased after every step of the process. The exfoliation efficiency in the Continuous protocol might decrease as the initial concentration of bulk h-BN in the

ethanol-water solvent decreases from 5 mg mL^{-1} to 4.71 mg mL^{-1} and 4.39 mg mL^{-1} at 1880 and 950 rpm centrifugation speed, respectively, compared to that in the Segmented protocol (5 mg mL^{-1}). This indicates that more exfoliated h-BN was obtained through the Segmented repetitive sonication centrifugation process.

The HRTEM images, presented in figures 2(b)–(e), were used to validate the exfoliation of h-BN nanosheets from bulk h-BN through imaging of the physical morphology. The HRTEM image of bulk h-BN (figure 2(b)) showed multilayered structures with a wide range of 10–96 layers and an average of 27 ± 20 nanosheets stacked in different directions. The exfoliation process significantly reduced the range of the layer numbers in the h-BN nanosheets, presented in figures 2(c)–(d), to 3–15 layers with an average of 9 ± 5 layers; the lowest layer numbers in the exfoliated h-BN nanosheets found through HRTEM images were three (3) layers (figure 2(c)). This overall decrease in layer thickness after the exfoliation provides evidence of the efficacy of these exfoliation processes.

Figure 2(d) shows high-resolution images of multiple closely stacked layers of one exfoliated h-BN nanosheet. The interlayer distance between two consecutive layers of h-BN nanosheets was measured to be 0.33 nm, which matches the previous literature [28, 67]. The Fast Fourier Transform image (FFT, figure 2(e); Inset) associated with figure 2(d) provides crystallographic information about the h-BN nanosheets. FFT converts the signal of the atoms' placement from a spatial domain in the HRTEM image to a frequency distribution of pixel intensity. The FFT image in the inset of figure 2(e) showcases 6 bright symmetric spots equidistant from the center and the nearby neighbors, indicating the six atoms in the hexagonal structure of h-BN nanosheets [68]. The position of these bright spots will be the same if the center axis is rotated 60° six times, indicating a six-fold symmetry. In other words, the six-fold symmetry corresponds to the hexagonal honeycomb structure of the h-BN nanosheet. The inverse FFT is performed on the FFT image to transform the processed frequency data back to spatial information (figure 2(e)). The white spots in figure 2(e) form the 'two atom-based rhombus-shaped unit cells' (marked as yellow rhombus) of the hexagonal 2D Bravais lattice pattern with a 120° angle. The distance between two neighbor white spots, i.e., arms of these unit cells, is estimated to be 0.24 nm from the plot profile added in the Supplementary Information (SI; figure S1). This is similar to the interatomic distance or lattice constant of h-BN of ∼(0.22–0.25) nm reported in previous literature [69–71]. Additionally, the angular measurements between the two directions of white dots were measured to be 118.2° using figure 2(e). These values follow the literature, indicating that these layers are part of h-BN nanosheets. From the d spacing and angular measurements obtained using the inverse FFT image in figure 2(e), the B—N bond length is calculated to be 1.39 Å, close to the 1.40–1.45 Å value reported previously [69, 71]. A geometric illustration of the basal plane of the exfoliated h-BN nanosheet has been added in figure 2(f) to summarize the lattice information discussed above.

Figures S2 and 3 show the low-magnification images (Bright field mode, 1 μm) that depict the lateral dimensions and shapes of bulk h-BN and exfoliated h-BN nanosheets from different exfoliation protocols. The bulk h-BN in figures S2(a) and S2(b) had larger (>1 μm) lateral-sized flakes stacked together. Both uniformly round (figure S2(a)) and irregularly shaped (figure S2(b)) bulk h-BN sheets were observed to be clustered together. Figures 3(a)–(c) correspond to the exfoliated nanosheets C3750, C1880, and C950 produced via the Continuous protocols, respectively, where 'C' designates the Continuous protocol, and the numbers correspond to the centrifugation speeds in rpm. Figures 3(d)–(f) are the S3750, S1880, and S950 nanosheets from the Segmented protocol. The h-BN nanosheets, corresponding to C3750 and S3750, obtained using 3750 rpm of centrifugation speed, appeared to be irregular in shape with lateral sizes smaller than those of bulk h-BN (figures 3(a) and (c)). They have smaller lateral sizes than nanosheets from 1880 and 950 rpm, indicating that the supernatant at higher centrifugation speed did contain nanosheets with smaller sizes.

The h-BN nanosheets from the 1880 rpm, i.e., C1880 and S1880, showed varying sizes and shapes (figures 3(b) and (e)). The h-BN nanosheets in C1880 and S1880 were smaller in lateral size (< 1 μm) than the bulk h-BN ones (figures S2(a) and S2(b)). These exfoliated h-BN nanosheets obtained are observed to be irregularly shaped (having sides and angles of differing values) flakes both spread out (figures 3(b) and (e)) and clustered form (Figures S2c and S2d). Some uniformly shaped exfoliated h-BN nanosheets were also found at 1880 rpm (Figure S2e). The h-BN nanosheets from the 950 rpm, i.e., C950 and S950 nanosheets, contained mostly spread-out irregularly shaped flakes (figures 3(c) and (f)). Similar to the exfoliated h-BN nanosheets from 1880 rpm, some uniformly round nanosheets were also observed at the low speed of 950 rpm (figure S2(f)). Figures 3(c) and (f) also showed a minuscule amount of aggregated h-BN structures in the exfoliated h-BN nanosheets. These images indicate that the Continuous and Segmented protocols produce h-BN nanosheets of similar size, shape, and structure at centrifugation speeds of 1880 rpm and below. Compared to the h-BN nanosheets obtained at 3750 rpm, those from 1880 and 950 rpm contained less aggregated and larger nanosheets (figure 3).

Lowering the centrifugation speed changes the lateral size and shape of the h-BN nanosheets being separated during centrifugation. However, the TEM images show slight differences in the exfoliated h-BN nanosheets obtained using 1880 and 950 rpm centrifugation speeds. The relative centrifugal forces for 3750, 1880, and 950 rpm were calculated to be 1572.19 × g, 395 × g, and 100.90 × g, respectively, using equation S1. The

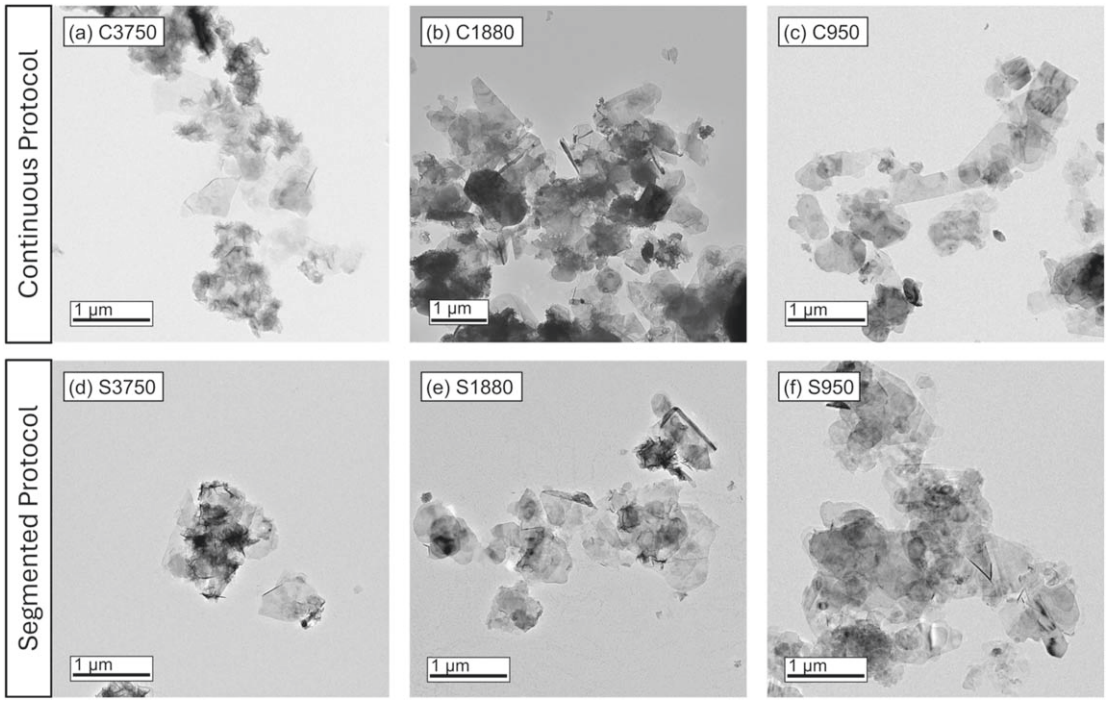

Figure 3. Low magnification TEM images of exfoliated h-BN nanosheets (a) C3750, (b) C1880, (c) C950, (d) S3750, (e) S1880, and (f) S950. The letters C and S correspond to the Continuous and Segmented protocols, while the subsequent numbers 3750, 1880, and 950 refer to the centrifugation speeds used to obtain the h-BN nanosheets.

difference in the forces applied during centrifugation speeds of 3750 and 1880 rpm with that of 950 rpm are 15.6 and 3.9-fold. As the force applied at 950 and 1880 rpm are closer compared to 3750, the lateral size range of the nanosheets might appear to be closer in both centrifugation speeds. C1880 and S1880 had lateral area ranges of 0.02–0.47 μm^2 and 0.01–0.68 μm^2, respectively (measured from figures 3(b) and (e)). On the other hand, C950 and S950 had wider lateral area ranges of 0.053–0.67 μm^2 and 0.01–0.8 μm^2, respectively (measured from figures 3(c) and (f)). Although the difference is relatively small, it is still present, indicating that these nanosheets are not exactly similar. Other studies using that liquid phase exfoliation process and different centrifugation speeds have already demonstrated that with higher centrifugation speed, the nanosheet layer number decreases [72–74]. Hence, another possibility is that nanosheets from 1880 and 950 rpm might have varying layer thicknesses despite the similar lateral size range.

Figure S3 compares the relative frequency distribution of the flake area of bulk h-BN and exfoliation h-BN nanosheets obtained from the Continuous and Segmented protocols. The TEM image of bulk h-BN in figure S2(a) was used for this analysis. The lack of adequate numbers of individual nanosheets in the TEM images of C3750 and S3750 (figures 3(a) and (d)) hindered calculating the lateral area distribution in these samples. The lateral area of the exfoliated h-BN nanosheets in figures 3(b), 3(c), 3(e), and 3(f) ranged from 0.01–0.8 μm^2 (Figure S3), while the lateral area of the bulk h-BN in figure S2(a) ranged from 0.021–1.69 μm^2. For the bulk h-BN, the average lateral area is measured to be $0.39 \pm 0.55\ \mu m^2$. For the exfoliated h-BN nanosheets, both protocols had an average lateral area less than the bulk h-BN. When compared between the two exfoliation protocols, the Continuous and Segmented protocols, the S1880 nanosheets had a lower average lateral area of $0.11 \pm 0.14\ \mu m^2$ (CI [0.06, 0.16] μm^2, SDM = 0.026) compared to that of C1880, $0.19 \pm 0.12\ \mu m^2$ (CI [0.15, 0.23] μm^2, SDM = 0.022). Similarly, nanosheets in S950 had a lower average lateral area of $0.13 \pm 0.16\ \mu m^2$ (CI [0.07, 0.19] μm^2, SDM = 0.029) compared to that of C950, $0.21 \pm 0.15\ \mu m^2$ (CI [0.06, 0.15] μm^2, SDM = 0.027).

Two-way ANOVA analysis and post hoc Tukey's test were performed to understand the significance of the effects of different exfoliation parameters (exfoliation process and centrifugation speed) and their interactions on the lateral size of the exfoliated h-BN nanosheets (table S1). However, irrespective of the exfoliation parameters, all the average lateral areas were placed in the same group, 'A' (table S1). This finding exhibits no statistical significance in the lateral area ($p > 0.05$) in nanosheets from both exfoliation protocols when the centrifugation speed is 1880 rpm or lower. As the centrifugation speed increased from 950 to 1880 rpm, the average value and the range of the lateral area of the exfoliated h-BN nanosheet decreased. This pattern indicates a further and significant reduction in the lateral area if the centrifugation speed increases to a higher level, such as 3750 rpm.

Figure S3 shows that C950 and S950 had a larger area distribution range than that in C1880 and S1880, respectively. This larger size distribution at 950 rpm centrifugation speed could be due to fewer amounts of larger nanosheets being precipitated with low centrifugation speed. Nonetheless, this difference is minimal to influence the lateral area of the h-BN nanosheets significantly. While 1880 and 950 rpm centrifugation speeds produce h-BN nanosheets of similar lateral area, the h-BN exfoliation yield is greater at the lower speed of 950 rpm (figure 2(a)). This indicates that the Segmented exfoliation protocol and 950 rpm centrifugation speed might be viable for producing smaller-sized h-BN nanosheets with a higher yield.

3.1.2. Chemical composition analysis

The HAADF-STEM image was used to investigate the structural configuration of the bulk h-BN at the atomic scale (figure S4(a)). Figure S4(b) shows the corresponding EDS spectra of the bulk h-BN HAADF-STEM image in figure S4(a), displaying the presence of boron (B), nitrogen (N), oxygen (O), carbon (C), and copper (Cu) peaks. The C and Cu presence was attributed to the TEM sample grid being a lacey carbon-coated Cu grid. The corresponding elemental composition in figure S4(c) for the HAADF-STEM image of the bulk h-BN (figure S4(a)) is primarily composed of B and N, with minimal O presence. Similarly, the HAADF-STEM image and EDS analysis graph for the exfoliated h-BN nanosheets from S950 are presented in figures S5(a) and S5(b), respectively. Figure S5(b) shows that the exfoliated h-BN nanosheets (figure S5(a)) had a similar elemental presence as the bulk h-BN (figure S4(b)). However, exfoliated nanosheets showed a much higher O presence in the elemental maps (figure S5(c)) than in the bulk h-BN (figure S4(c)). This indicates possible chemical composition changes during exfoliation where the −OH group from the exfoliation solvent (water) is attached to the exposed edges of the h-BN nanosheets (figure S5(c)) [75].

Based on the EDS and elemental mapping, further analysis was conducted by XPS to analyze the chemical states and bond composition of different elements in the exfoliated h-BN nanosheets obtained from the two protocols. Figures obtained from this analysis have been added to the SI (figures S6–12). The XPS survey scans (figure S6) showed the presence of B, N, and O as the main elements, with some C, Si, Mg, and Na as impurities in all the exfoliated h-BN nanosheets. While the C is also present in the unprocessed bulk h-BN, the sources of the other impurity elements could be adsorption from the exfoliant solvents or air exposure [27, 76, 77]. The atomic percentages of the B, N, and O were calculated from the XPS survey scans after removing the interferences from the impurities [75]. Comparison of B, N, and O peaks from the survey scan showed higher atomic % of O and lower atomic % of B and N in the exfoliated h-BN nanosheets of the Continuous and Segmented protocols than the bulk h-BN (figure S7). This higher O presence in exfoliated h-BN nanosheets from both protocols might come from the water used in the exfoliant solvent during the exfoliation [26, 35, 78]. The B: N ratio increased slightly from 1.026 in the bulk h-BN to 1.155–1.187 and 1.1066–1.286 for the exfoliated nanosheets of the Continuous and Segmented protocol, respectively. Only for the C1880, the B: N ratio remained at 1.022. This increase in the atomic ratio and higher O presence in the exfoliated h-BN nanosheets compared to the bulk h-BN indicate possible N substitution by O during exfoliation [28, 79]. The Segmented protocol nanosheets contained 6.93, 6.21, and 0.59% more oxygen presence than the Continuous protocol nanosheets for centrifugation speeds 3750, 1880, and 950 rpm, respectively (figure S7). This indicates that h-BN nanosheets were more hydroxylated when the Segmented protocol was followed for exfoliation.

The nanosheets from C3750 and S3750, obtained using the highest centrifugation speed, had the largest O contents (32.82% for C3750 and 35.1% for S3750) compared to those obtained from the lower centrifugation speeds (figure S7). With high centrifugation speed, the nanosheets separated in the supernatant would be more exfoliated and contain reduced layers and smaller lateral sizes. Mechanical energy from sonication might cause the tearing effect to produce smaller-sized h-BN nanosheets [26]. This would result in a higher number of exposed edges in the exfoliated nanosheets from higher centrifugation speeds. More −OH bonds might replace the nitrogen on the edges and form B−OH bonds on the exfoliated nanosheets.

The B 1s scans of bulk h-BN and exfoliated h-BN nanosheets (figures 4(a), (b), and S8) were fitted to two main peaks: 190.25 ± 0.10 eV for B−N [80–82] and 191.75 ± 0.36 eV for B−OH (table S2) [13, 14]. The C3750 and S3750 contained another peak attributed to B−O, positioned at 194.26 ± 0.08 eV [83]. The gradual shift from 190.25 eV for B−N to 194.26 eV for B−O is due to the electronegativity difference among the element or functionalized group attached to the boron atoms [84]. While the −OH group is more electronegative than N, O in B−O contains a higher negative oxidation state. This higher negative oxidation state resulted in a higher binding energy of 194.26 eV [84]. Due to the addition of new chemical states, the B 1s spectra scans of exfoliated nanosheets (figures 4(b) and S8) contained broader and asymmetric peaks than those of the bulk h-BN (figure 4(a)).

Figures 4(c) and (d) compare the boron bond composition on the surface of the h-BN nanosheets obtained from the Continuous and Segmented protocols, respectively, based on the B1s spectrum area analysis (figures 4(a), (b), and S8). The amount of B−N bond (23.61–64.48%) was less in the exfoliated nanosheets from both protocols compared to the bulk h-BN (91.35%) (figures 4(c) and (d)). This indicated that B atoms in the

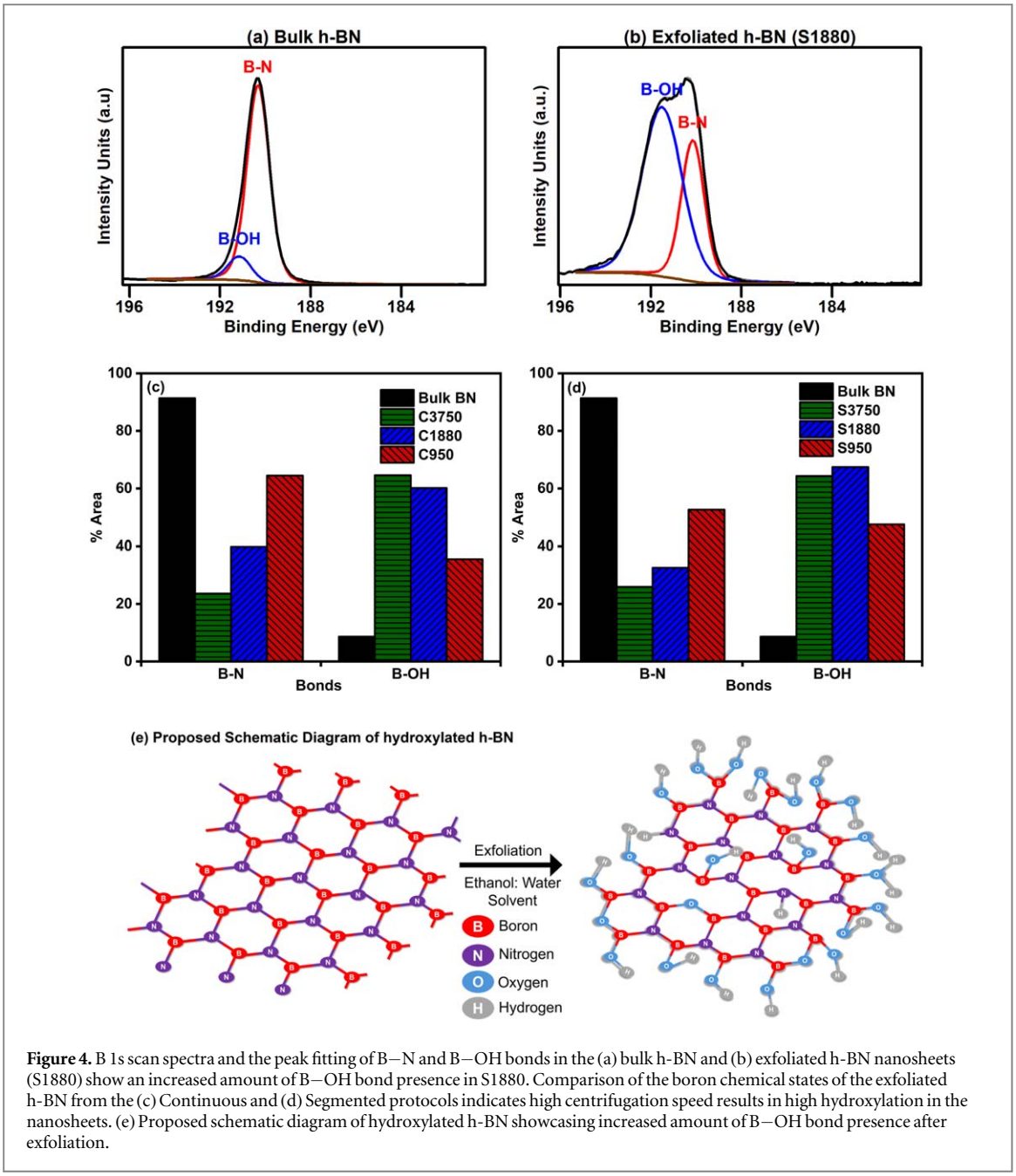

Figure 4. B 1s scan spectra and the peak fitting of B−N and B−OH bonds in the (a) bulk h-BN and (b) exfoliated h-BN nanosheets (S1880) show an increased amount of B−OH bond presence in S1880. Comparison of the boron chemical states of the exfoliated h-BN from the (c) Continuous and (d) Segmented protocols indicates high centrifugation speed results in high hydroxylation in the nanosheets. (e) Proposed schematic diagram of hydroxylated h-BN showcasing increased amount of B−OH bond presence after exfoliation.

bulk h-BN are predominantly attached to N atoms. Compared to that, h-BN nanosheets from both protocols showed a higher extent of hydroxylation (35.52–67.44%), indicating that B was also attached to −OH groups. This provides evidence of chemical property change of h-BN nanosheets via −OH functionalization groups substituting the nitrogen in the exfoliated nanosheets during the sonication [28]. Elemental maps of O content in the bulk and exfoliated h-BN nanosheets in figures S4(c) and S5(c), respectively, corroborated similar findings, as higher amounts of O were spatially distributed in the latter exfoliated samples (figure S5(c)).

Among the exfoliated h-BN nanosheets, the Segmented protocol samples showed a similar amount of B−OH bond presence as the Continuous protocol samples for 3750 and 1880 rpm centrifugation speed. The exfoliated nanosheets in C3750 and C1880 had 64.6% and 60.16% of the peak area associated with B−OH, respectively, similar to the Segmented protocol ones, S3750 (64.35%) and S1880 (67.44%) (figure 4(d)). However, with a decrease in centrifugation speed to 950 rpm, the hydroxylation percentage decreased to 35.52% and 47.54% for the C950 and S950 nanosheets, respectively (figures 4(c) and (d)). Furthermore, the nanosheets from S950 had 12.02% more area corresponding to the B−OH bond than the ones from C950. This indicates that the Segmented protocol nanosheets have higher B−OH bond presence at low centrifugation speed than the other protocol. This finding is also supported by the atomic % comparison obtained from the XPS survey scan (figure S7). This increase in hydroxylation could be attributed to the higher number of exposed edges resulting from nanosheets with more layers in the Segmented protocol (figure 2). A similar extent of hydroxylation as

S950 and C950 had been reported previously, where heating at high temperatures (800 °C–1000 °C) was introduced as a pretreatment before the sonication and centrifugation steps of exfoliation [28]. The exfoliated nanosheets might have mostly boron atoms on the edges after tearing due to thermodynamically favorable ammonia release in the solvent [26, 85]. This would make the nanosheets more accessible for the B-OH bonds. While slight to no N defects might be present in the pristine bulk h-BN, the sonication step in the exfoliation process might induce N defect in the h-BN lattice. The O or -OH might also occupy the defect space in the nanosheet by bonding with the neighboring boron atoms [26, 76, 86, 87], leading to slight changes in the structure of hydroxylated h-BN nanosheets. Figure 4(e) provides a schematic illustration of the proposed hydroxylated structure.

Although table S1 shows no significant difference in the lateral area distribution of exfoliated h-BN nanosheets obtained from 1880 and 950 rpm centrifugation speed, C950 and S950 did contain 5.56% and 3.125% more nanosheets with larger lateral areas than C1880 and S1880, respectively (figure S3). With hydroxylation happening mainly on the exposed edge of the nanosheets, these larger nanosheets might provide more sites for the −OH bond attachment. However, with the lateral size increasing, the proportion of exposed edges to the lateral area decreases. As B−OH bonds are primarily on the edge, the ratio of B−OH and B−N declines. Due to this decline, a decreasing trend of B−OH bond presence with lower centrifugation speeds was observed.

The N 1s scans of exfoliated h-BN nanosheets (figure S9) were fitted to two main peaks: 397.85 ± 0.07 eV for N−B [70, 84] and 399.45 ± 0.21 eV for N−H (table S2) [70, 84]. The sharp and symmetric N 1s peak in bulk h-BN (figure S9(a)) became broader and asymmetric in all the exfoliated h-BN nanosheets due to the introduction of N−H bonds (figures S9(b)–S9(g)). While no N−H bond was found in the bulk h-BN, exfoliated h-BN from both protocols revealed the presence of this N chemical composition. The N−H bond might result from hydrogen atoms binding to the exposed nitrogen on the torn-down h-BN nanosheets during hydrolysis [70].

The amount of N−H bond in the exfoliated h-BN nanosheets increased with increasing centrifugation speed for both protocols (figure S10). This bond could be attributed to 71.40% and 67.08% of the N 1s spectra of the h-BN nanosheets exfoliated at 3750 rpm using the Continuous and Segmented protocols, respectively. At 950 rpm, this composition presence reduced to 35.01 and 44.22% for the exfoliated nanosheets from the Continuous and the Segmented protocol, respectively. Similar to the trend of B−OH, the decrease of N−H bonds with decreasing centrifugation speed could be due to the decreasing ratio of the exposed edge and the lateral area of the nanosheets. Moreover, S950 contained 9.21% more area corresponding to the N−H bond than the C950. This finding corroborated the higher B−OH bond presence in the Segmented protocol nanosheets at 950 rpm than in Continuous protocol nanosheets (figure 4(d)). This increase in N−H bonds could be attributed to the higher number of exposed edges resulting from nanosheets with more layers in the Segmented protocol (figure 2). Furthermore, the pH of the h-BN dispersion before sonication was measured to be 7.81 ± 0.03. After exfoliation, the pH level increased to 9.11 ± 0.02. This increased pH could be due to the transfer of N atoms from the exposed edges of the freshly torn nanosheets into the water during sonication and subsequently forming ammonia [26]. This indicates that nitrogen atoms on the exposed edges of the exfoliated h-BN nanosheets either formed N−H bonds or entered the solvent media as ammonia after sonication. This ammonia might volatilize into the surrounding environment during the drying step, and if the concentration is sufficiently high, this release could pose a health risk.

The O 1s spectrum of bulk h-BN (figure S11(a)) was fitted at 531.98 ± 0.25 eV for either C−O [88, 89] or Si−O [89, 90]. The low binding energy peak can be due to possible surface contamination. In the exfoliated h-BN nanosheets (figures S11(b)–(g)), there was an additional peak (figure S11) at 533.68 ± 0.33 eV for O−B (table S2) [76, 88, 90]. The C 1s spectra signal was assigned to three different peaks, C−C, C−O−C, and C=O, at around 284.4, 286, and 288 eV, respectively, for the bulk and exfoliated h-BN nanosheets. Figure S11(a) shows the absence of the O−B bond in the bulk h-BN, indicating no hydroxylation. Conversely, this bond presence increased in the exfoliated h-BN nanosheets from both exfoliation protocols with increasing centrifugation speed (figure S12) aligning with the B−OH and N−H bond formation data from the B1s and N 1s spectra, respectively (figures 4 and S7). This indicates a higher amount of O attachment to the exfoliated nanosheet surface.

3.2. Surface charge property of exfoliated h-BN nanosheets

3.2.1. Effect of dispersion media on surface charge

When dispersed in DI water, the h-BN nanosheets obtained from both protocols showed negative surface charges greater than the aggregation threshold of −30 mV (figures 5(a) and (b)) [91]. Therefore, the surface charge of the h-BN nanosheets in DI water ranged between −30.71 ± 0.55 to −34.48 ± 1.71 mV for the Continuous protocol and between −31.6 ± 1.51 to −35.01 ± 0.92 mV for the Segmented protocol (table S3).

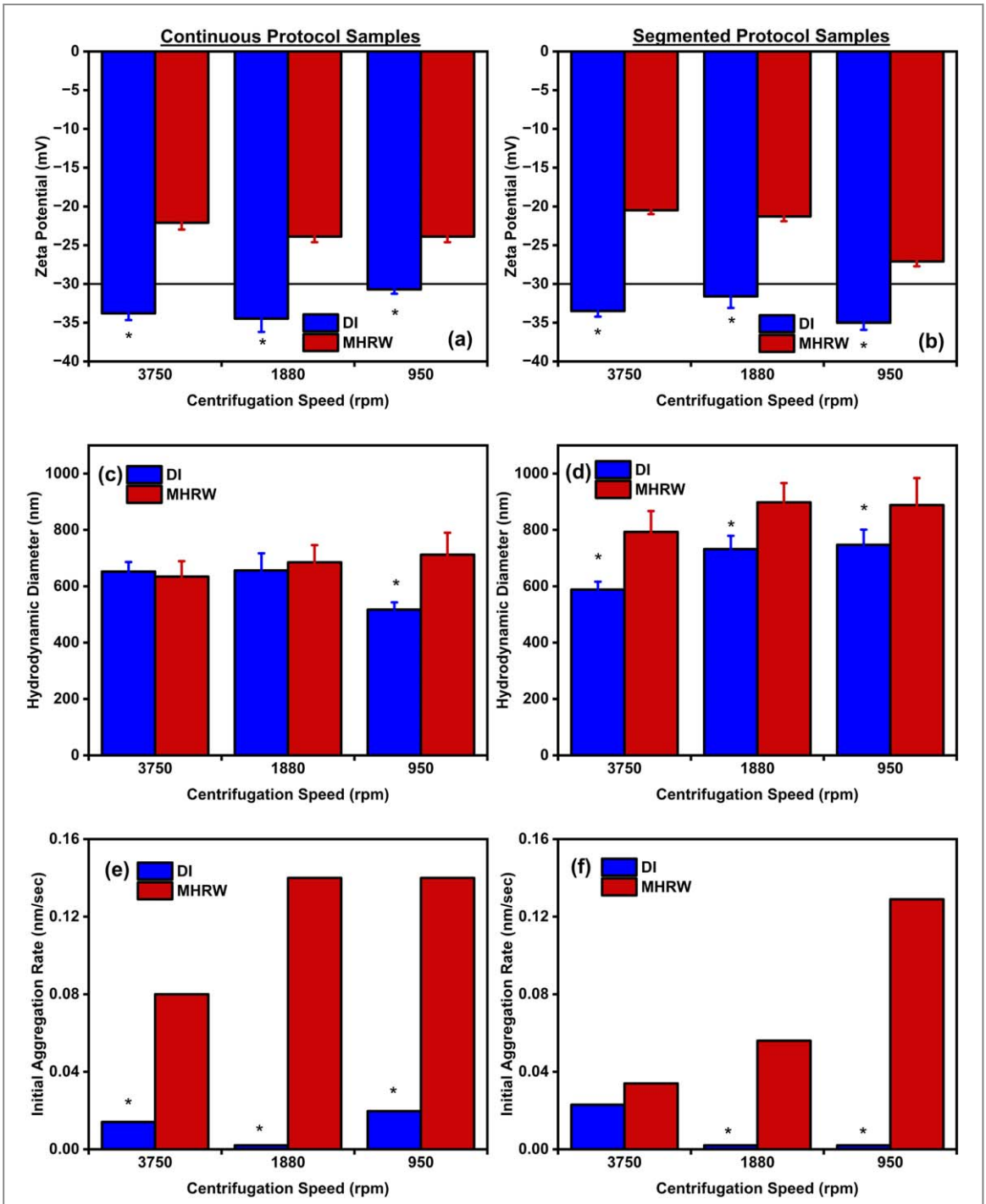

Figure 5. Surface charge or zeta potential, average hydrodynamic diameter, and initial aggregation rates of the exfoliated h-BN nanosheets obtained from (a), (c), (e) Continuous and (b), (d), (f) Segmented protocols, dispersed in DI and MHRW as a function of centrifugation speeds. The surface charge decreases for all h-BN nanosheets in the presence of ions. The hydrodynamic diameter of the nanosheets increases with a decrease in centrifugation speed in both protocols. The Continuous protocol nanosheets show higher initial aggregation rates than the Segmented protocol nanosheets.

These measurements are consistent with the zeta potential values of exfoliated h-BN nanosheets reported in the literature that range from −26 to −52 mV [28, 35, 92, 93]. These high negative zeta potential values (>−30 mV) indicate that the colloidal dispersions of h-BN nanosheets are stable, possibly due to a high electrostatic barrier against aggregation between the exfoliated h-BN [62, 91]. However, when the h-BN nanosheets were dispersed in the MHRW, their surface charge range decreased to -22.08 ± 0.89 to -23.87 ± 0.71 mV for the Continuous protocol and -20.49 ± 0.49 to -27.07 ± 0.62 mV for the Segmented protocol. These measurements are also quite close to the zeta potential values of hydroxylated h-BN nanosheets in the presence of similar concentrations of ions previously reported [35]. The salt ions present in the 5.16 mM ionic strength MHRW suspension decrease the amount of charge available on the slipping plane of the nanosheet surface. This, in turn,

compresses the electric double layer and reduces the zeta potential of the h-BN nanosheets [35]. A three-way ANOVA analysis was also employed here to understand the contributing effects of exfoliation protocols, centrifugation speed, dispersion media, and their interactions on the surface charge of the exfoliated h-BN nanosheets. The observed surface charge differences in the h-BN nanosheets dispersed in DI water and MHRW were statistically significant ($p < 0.05$), irrespective of the exfoliation protocols and centrifugation speeds used to produce the nanosheets. Tukey's test surface charge means comparison presented in table S4 classifies the zeta potential of h-BN nanosheets dispersed in DI water to the groups 'E,' 'F,' and 'G' and h-BN nanosheets dispersed in MHRW to the groups 'A,' 'B,' 'C,' and 'D'. These different letter groups indicate a statistically significant difference in surface charge based on dispersion media. This finding suggests that ions in the aqueous media significantly influence the surface charge of h-BN nanosheets, leading to decreased stability.

3.2.2. Effect of exfoliation protocol on surface charge

For centrifugation speeds of 3750 and 1880 rpm, h-BN nanosheets from the Continuous protocol were more negatively charged than those from the Segmented protocol, irrespective of the dispersion media (table S3). Conversely, for the 950 rpm speed, h-BN nanosheets from the Segmented protocol carried more negative charge than those from the Continuous protocol. This corroborates the findings from figures 4(c) and (d), where nanosheets from S950 contained 12.5% more −OH bonds than the C950 one. With more −OH groups attached to the Segmented protocol h-BN nanosheets, they have a higher negative surface charge than those from the Continuous protocol [94]. Hence, S950 would be colloidally more stable than the C950. Table S4 categorizes the zeta potential of the C3750 and S3750 h-BN nanosheets in similar groups 'F' when dispersed in DI water, which is expected given the similarity in the exfoliation protocols used to obtain these C3750 and S3750 h-BN nanosheets. In both protocols, Continuous and Segmented, the centrifugation speed used for the first 3 cycles of exfoliation is 3750 rpm. This indicates the degree of exfoliation for C3750 and S3750 at this stage is likely similar due to the total identical mechanical forces applied. Except for this case, the exfoliation protocol significantly influences the surface charge of the exfoliated h-BN nanosheets. In summary, h-BN nanosheets obtained from the Continuous protocol have a greater surface charge at higher centrifugation speeds (1880 rpm). However, the h-BN nanosheets from the Segmented protocol would have a higher surface charge at the lowest centrifugation speed of 950 rpm.

3.2.3. Effect of centrifugation speed on surface charge

The surface charges of the h-BN nanosheets became more negative with decreasing centrifugation speed, regardless of exfoliation protocol and dispersion media (figures 5(a) and (b)). However, in DI water dispersion, h-BN nanosheets from C3750 and C1880 contained similar surface charges (Grouped as 'G' in table S4). In MHRW dispersion, S3750 and S1880 h-BN nanosheets were classified as the group 'A,' and C1880 and C950 were classified as the group 'C,' indicating no statistical significance in their surface charges. S950 nanosheets contained the highest negative surface charges in both dispersion media among all exfoliated nanosheets. S950 contained 6.25% more nanosheets than S1880, with a lateral area larger than 0.25 μm^2 (figure S3). These larger nanosheets in S950 might contain a higher number of exposed edges than those in S1880. During sonication, −OH groups attach to these exposed edges of the h-BN nanosheets. With more −OH groups attached to B sites via favorable adsorption, the surface of the h-BN nanosheets becomes more negatively charged [95, 96]. For this reason, h-BN nanosheets obtained using a low centrifugation speed of 950 rpm are colloidally more stable than those produced using the higher centrifugation speeds.

3.3. Colloidal stability of exfoliated h-BN nanosheets

3.3.1. Effect of dispersion media on colloidal stability

The time dependent hydrodynamic diameter profiles of bulk h-BN and h-BN nanosheets obtained from all centrifugation speeds, determined using the TRDLS technique, remained stable over time, within narrow standard deviations when dispersed in DI water (figures S13(a) and S13(c)). However, bulk h-BN was observed to have a larger hydrodynamic diameter with a wider standard deviation in MHRW dispersion with a slightly decreasing trend (figure S13(b)). This trend is due to the large bulk h-BN aggregating to bigger nanosheets and settling down with faster Brownian motion than the exfoliated nanosheets. On the contrary, in MHRW dispersion, the hydrodynamic diameters of h-BN nanosheets increased gradually with time and had wider standard deviations for all centrifugation speeds (figure S13(d)). These results indicated decreased colloidal stability of the exfoliated h-BN nanosheets in MHRW dispersion compared to those in DI (figure S13(c)) [35]. This colloidal behavior difference between DI water and MHRW dispersions can be attributed to the decrease in the surface charge of the h-BN nanosheets in the presence of ions in the case of MHRW (figures 5(a) and (b)). A decrease in zeta potential reduces the electrostatic repulsion in the h-BN nanosheets. As a result, the nanosheets become more susceptible to aggregation, leading to an increase in their hydrodynamic diameter [35, 56].

Figures 5(c) and (d) present the average initial hydrodynamic diameter of the exfoliated h-BN nanosheets dispersed in DI water and MHRW as a function of the centrifugation speeds for the Continuous and Segmented protocols, respectively (also provided as table S5). The average hydrodynamic diameters of the h-BN nanosheets obtained from the Continuous and the Segmented protocols are much smaller than the average hydrodynamic diameter of bulk h-BN (2259 $\pm$ 694 nm) dispersed in DI water (figure S13(a)). While the bulk h-BN dispersion demonstrated a wide particle size distribution with a polydispersity index (PDI) of 0.93 $\pm$ 0.15, the exfoliated h-BN nanosheets from both protocols had narrow particle size distribution ranges with lower PDI (table S6). This difference in hydrodynamic diameter and PDI values in the bulk and exfoliated h-BN provided further evidence of exfoliation, supporting the reduced-sized h-BN nanosheets in the TEM images in figures 3 and S2. The PDI decreased with increased centrifugation speed for the Segmented protocol h-BN nanosheets. This indicated the nanosheet size distribution was broader for low centrifugation speed. This is expected as larger nanosheets are removed at high centrifugation speed. However, the opposite trend is observed for the Continuous protocol h-BN nanosheet samples. In this protocol, C1880 was produced from the precipitate of C3750, and C950 was produced from the precipitate of C1880. The bulk h-BN underwent repeated sonication throughout the eight recycling steps, gradually producing uniform nanosheets with low PDI values (Final precipitate PDI 0.567 $\pm$ 0.289). Starting a new cycle with an h-BN precipitate of lower PDI than the original bulk h-BN further enhanced nanosheet uniformity. Hence, the PDI decreased from C3750 to C950 (table S6). Compared to DI water, the average hydrodynamic diameters of h-BN nanosheets increased when dispersed in MHRW. The h-BN nanosheets also had a wider diameter range in MHRW dispersion, for both protocols (table S5).

A three-way ANOVA analysis was employed to understand the effects of different factors (exfoliation protocol type, centrifugation speed, and dispersion media) and their interactions on the colloidal stability of the exfoliated h-BN nanosheets. Table S7 provides the statistical significance results associated with the average hydrodynamic diameter of h-BN nanosheets. Except for C3750, all other h-BN nanosheets from both exfoliation protocols showed significantly higher average hydrodynamic diameter when dispersed in MHRW than in DI water ($p < 0.05$). While C3750 showed the opposite trend in its average hydrodynamic diameter (i.e., higher in DI water than in MHRW), the difference in these values was not statistically significant as they were designated in the same group 'F' for means comparison in table S7 ($p > 0.05$). This suggests that exfoliated h-BN nanosheets exhibit significantly reduced stability when dispersed in MHRW compared to DI water, irrespective of exfoliation protocols and centrifugation speeds. The increase in the average hydrodynamic diameter in MHRW dispersion is attributed to nanosheet aggregation in the presence of ions. Figures 5(a) and (b) show a decrease in surface charge in the presence of ions. These ions in the water induce a double-layer compression effect on the h-BN nanosheets, prompting lessened electrostatic repulsion and subsequent aggregation [35, 62].

The hydrodynamic diameter was also measured for 72 h for S1880 to compare the stability of the nanosheets as a function of time when dispersed in DI water and MHRW (figure S14). The nanosheet diameters were much more stable in DI water over this time than in MHRW. The nanosheet diameter increased nearly six times after 72 h in the presence of the ions in MHRW. It is deduced from observing this information that exfoliated h-BN nanosheets would aggregate to a certain degree in the presence of ions.

3.3.2. Effect of exfoliation protocol on colloidal stability

When comparing the nanosheets from two exfoliation protocols dispersed in MHRW, all the Segmented protocol nanosheets had larger hydrodynamic diameters than the Continuous protocol ones ($p < 0.05$). However, when dispersed in DI water, only S1880 and S950 had larger nanosheet hydrodynamic sizes than C1880 and C950, respectively (table S5). For MHRW dispersion, the hydrodynamic diameters of the nanosheets from the Segmented protocol are grouped into A and B. In contrast, those of the Continuous protocol are placed into E and F (table S4). Furthermore, the Segmented protocol nanosheets are classified under groups C and G for DI water dispersions. In contrast, exfoliated h-BN from Continuous protocol dispersed in DI water are placed into groups F and H (table S4). Being categorized into different groups indicates that the effect of the exfoliation protocol on the colloidal stability of the exfoliated h-BN nanosheets is statistically significant. According to figures 5(c) and (d), h-BN nanosheets from the Continuous protocol had significantly smaller hydrodynamic diameters than those from the Segmented protocol, irrespective of dispersion media. This data suggests that h-BN nanosheets obtained from the Continuous protocol might be more resistant to aggregation and maintain a more stable colloidal dispersion in MHRW than those obtained from the Segmented protocol.

3.3.3. Effect of centrifugation speed on colloidal stability

The hydrodynamic diameter of h-BN nanosheets generally increased with the reduction in centrifugation speed irrespective of dispersion media and exfoliated protocols (figures 5(c) and (d)) [23, 45]. As seen in figure S3, some nanosheets with larger lateral areas are produced with a slower centrifugation speed. Because of these larger nanosheets, the average hydrodynamic diameter also increases with a decrease in centrifugation speed,

irrespective of suspension media (table S5). However, the average hydrodynamic diameters of C3750 and C1880 dispersed in DI water were not significantly different (Categorized as group 'F' in table S6, $p > 0.05$). Table S6 also classifies the S1880 and S950 in group 'C' when dispersed in DI water and group 'A' in MHRW ($p > 0.05$). This indicates that h-BN nanosheets obtained from Segmented protocol with centrifugation speed below 1880 rpm exhibit similar colloidal behavior, while nanosheets obtained from Continuous protocol above 1880 rpm exhibit similar behavior.

The TRDLS measurement also recorded the hydrodynamic diameter distribution range of exfoliated h-BN nanosheet when dispersed in DI water, providing insights into particle size distribution at various centrifugation speeds (figure S15). Nanosheets from 950 rpm demonstrated wider particle size distribution than the other centrifugation speeds for both exfoliation protocols. All the size distribution histograms were right-skewed, indicating a higher prevalence of nanosheets with smaller hydrodynamic diameters. For both protocols, nanosheets from 3750 rpm speed contained the highest nanosheet amount (C3750-20.3% and S3750-24.6%) with a hydrodynamic diameter range of 342–396.1 nm. This peak frequency shifted slightly to the 396.1–458.7 nm range for nanosheets collected at the lowest speed of 950 rpm (C950-16.5% and S950-18.7%). However, the maximum relative frequency differences between the Continuous and Segmented exfoliation protocols for the same hydrodynamic diameter were only 4.3, 5, and 2.2% for 3750, 1880, and 950 rpm centrifugation speeds, respectively. These minimal differences indicate that particle size distributions are similar across the exfoliation protocols regardless of the centrifugation speeds used. The area distribution histogram analysis in figure S3 corroborates this finding. Furthermore, this evidence supports the claim that using the Segmented protocol with a lower centrifugation speed for h-BN exfoliation is an effective strategy for achieving a high h-BN nanosheet yield as both protocols have minimal difference in the nanosheet size.

The h-BN nanosheets obtained from the 3750 rpm centrifugation speed, C3750 and S3750, showed negligible aggregation rates of 0.02 and 0.04 nm sec^{-1}, respectively, in DI water dispersion (figure 5(e)). On the other hand, initial aggregation rates for h-BN nanosheets in MHRW ranged from 0.03 to 0.14 nm sec^{-1} (figure 5(f)), indicating that ions in MHRW induce slight aggregation for h-BN nanosheets [35]. When dispersed in MHRW, h-BN nanosheets obtained from the Segmented protocol had lower aggregation rates than those obtained from the Continuous protocol. However, in both cases, the h-BN nanosheets obtained from lower centrifugation speeds had significantly higher initial aggregation rates than those from higher centrifugation speeds.

In summary, the average hydrodynamic diameter indicates that h-BN nanosheets from the Continuous protocol are more stable than those of the Segmented Protocol in MHRW dispersion. Conversely, the comparatively lower initial aggregation rate in figure 5(f) supports the Segmented samples to be more stable. Thus, surface charge might play a major role in determining the colloidal stability of the h-BN nanosheets. This is also supported by the higher hydroxylation of the h-BN nanosheets from the Segmented protocol than those from the Continuous protocol, as observed in figures 4(c) and (d). While for the Continuous protocol, h-BN nanosheets from high centrifugation speed show higher colloidal stability in DI water and MHRW dispersions, for the Segmented protocol, the nanosheets from low centrifugation speed show higher overall colloidal stability (figures 5(a) and (b)).

4. Conclusions

Two repetitive sonication centrifugation exfoliation processes using an ethanol-water solvent were developed to increase the exfoliation yield of h-BN nanosheets. Reusing unexfoliated h-BN precipitate in the Segmented protocol with only three cycles and 950 rpm centrifugation speed performed better with 22% nanosheet exfoliation yield than the Continuous protocol with nine cycles. The physical morphology of the nanosheets remained similar below 1880 rpm but showed slight aggregation at 3750 rpm. Sonication in ethanol-water solvent induced hydroxyl functionalization in these exfoliated h-BN nanosheets, but hydroxylation decreased with lower centrifugation speeds for both protocols. Decreasing the centrifugation speed is a tradeoff between yield and hydroxylation. If hydroxylated h-BN nanosheets of small lateral size and layer number are preferred, it is recommended to use centrifugation speed $\geqslant$ 950 rpm. The colloidal stability of these exfoliated h-BN in aqueous media was also focused on in this study. The initial aggregation rate indicated that h-BN nanosheets from the Segmented protocol were more stable than those of the Continuous protocol in MHRW dispersion. In both protocols, nanosheets obtained at 950 rpm exhibited a greater aggregation tendency in MHRW dispersion compared to those produced at higher speeds of 3750 rpm.

Water chemistry parameters such as pH, ionic strength, and natural organic matter presence play an important role in controlling the surface charge and aggregation behavior of nanomaterials. This, in turn, has influenced their contaminant removal capacity for water treatment [64]. The varying aggregation rate, surface charge, and hydrodynamic size of different exfoliated nanosheets might influence their performance in water

remediation. Depending on the extent of water chemistry impact, these variations might affect their suitability for environmental applications. The freshwater salinity, measured less than 500 ppm, closely approximates the 5.16 mM ionic strength of MHRW, indicating comparable conditions in terms of ionic strength [97]. If released into the environment, h-BN nanosheets are likely to be transported from their source before settling downstream, potentially leading to prolonged exposure to aquatic organisms [35]. Depending on the surrounding water chemistry and their aggregation behavior, h-BN nanosheets can remain suspended in water or deposited in sediment. Nanosheets accumulated in the sediment zone can encounter benthic organisms such as nematodes, while suspended ones can interact with organisms such as photosynthetic algae [98, 99]. So, the potential toxicity of h-BN nanosheets to these organisms might depend on their bioavailability. Exposure of h-BN to both of these organisms for up to 72 h has been reported to inhibit growth, decrease life span, and increase oxidative stress levels in the presence of high ionic strength of 21 mM [99, 100]. However, this elevated ionic strength might not accurately reflect real-life scenarios. To fully understand the environmental implications of h-BN release in natural aquatic systems, it is essential to consider the characteristics of the nanosheets produced during their synthesis, as well as their behavior in comparable aqueous environments. This work provides insights into the effects of the exfoliation process on the characteristics and colloidal stability of h-BN nanosheets in environmentally relevant aqueous media. This information will further assist in understanding the water remediation efficiency of h-BN nanosheets along with their fate, transport, and toxicity to evaluate their suitability for environmental applications.

Acknowledgments

This study is supported by a collaborative research grant from National Science Foundation Nanoscale Interaction Program (NSF award number CBET-2324853 to Nirupam Aich and CBET-2228033 to Olga Tsyusko and Isabel C. Escobar). The research was performed in part in the Nebraska Nanoscale Facility: National Nanotechnology Coordinated Infrastructure and the Nebraska Center for Materials and Nanoscience (and/or NERCF), which are supported by the National Science Foundation under Award ECCS: 2025298, and the Nebraska Research Initiative. We thank Dr Xingzhong 'Jim' Li from the NCMN Electron Nanoscopy Instrumentation Facility for his assistance with STEM imaging. We also thank Dr Steve Michalski from the NCMN Physical Properties Facility for his assistance with XPS analysis.

Conflicts of interest

The authors declare no competing interests that could have influenced the reported work above.

Data availability statement

We created two novel processes for 2D nanomaterial exfoliation, and we intend to file an invention disclosure at this time for our methods. The data that support the findings of this study are available upon reasonable request from the authors.

ORCID iDs

Nirupam Aich https://orcid.org/0000-0003-1896-8127

References

[1] Gonzalez Ortiz D, Pochat-Bohatier C, Cambedouzou J, Bechelany M and Miele P 2018 Exfoliation of hexagonal boron nitride (h-BN) in liquide phase by ion intercalation *Nanomaterials* **8** 716 https://mdpi.com/2079-4991/8/9/716
[2] Duan L *et al* 2020 Efficient photocatalytic PFOA degradation over boron nitride *Environmental Science & Technology Letters* **7** 613–9
[3] Zhou H *et al* 2014 High thermal conductivity of suspended few-layer hexagonal boron nitride sheets *Nano Res.* **7** 1232–40
[4] Kidambi P R, Chaturvedi P and Moehring N K 2021 Subatomic species transport through atomically thin membranes: present and future applications *Science* **374** eabd7687
[5] Falin A *et al* 2017 Mechanical properties of atomically thin boron nitride and the role of interlayer interactions *Nat. Commun.* **8** 15815
[6] Ciofani G, Danti S, Genchi G G, Mazzolai B and Mattoli V 2013 Boron nitride nanotubes: biocompatibility and potential spill-over in nanomedicine *Small* **9** 1672–85
[7] Hua Li L, Chen Y, Cheng B-M, Lin M-Y, Chou S-L and Peng Y-C 2012 Photoluminescence of boron nitride nanosheets exfoliated by ball milling *Appl. Phys. Lett.* **100** 1–4
[8] Yuan S *et al* 2018 Air-stable room-temperature mid-infrared photodetectors based on hbn/black arsenic phosphorus/hBN heterostructures *Nano Lett.* **18** 3172–9
[9] Kenry and Lim C T 2017 Biocompatibility and nanotoxicity of layered two-dimensional nanomaterials *Chem. Nano. Mat.* **3** 5–16

[10] Li J et al 2013 Activated boron nitride as an effective adsorbent for metal ions and organic pollutants Sci. Rep. 3 3208
[11] Bangari R S and Sinha N 2019 Adsorption of tetracycline, ofloxacin and cephalexin antibiotics on boron nitride nanosheets from aqueous solution J. Mol. Liq. 293 111376
[12] Liu T et al 2019 Few-layered boron nitride nanosheets as superior adsorbents for the rapid removal of lead ions from water J. Mater. Sci. 54 5366–80
[13] Duan L et al 2023 Insight into the key role of oxygen dopants over ball-milled boron nitride for efficient degradation of PFOS alternative 6:2 fluorotelomer sulfonic acid J. Hazard. Mater. 445 130419
[14] Duan L et al 2022 Titanium oxide improves boron nitride photocatalytic degradation of perfluorooctanoic acid Chem. Eng. J. 448 137735
[15] Chen Z et al 2017 Graphene-like boron nitride modified bismuth phosphate materials for boosting photocatalytic degradation of enrofloxacin J. Colloid Interface Sci. 492 51–60
[16] Singh B, Singh K, Kumar M, Thakur S and Kumar A 2020 Insights of preferred growth, elemental and morphological properties of BN/SnO_2 composite for photocatalytic applications towards organic pollutants Chem. Phys. 531 110659
[17] Di J et al 2016 Advanced photocatalytic performance of graphene-like BN modified BiOBr flower-like materials for the removal of pollutants and mechanism insight Appl. Catalysis B 183 254–62
[18] Naclerio A E and Kidambi P R 2023 A review of scalable hexagonal boron nitride (h-BN) synthesis for present and future applications Adv. Mater. 35 2207374
[19] Molaei M J, Younas M and Rezakazemi M 2021 A comprehensive review on recent advances in two-dimensional (2D) hexagonal boron nitride ACS Applied Electronic Materials 3 5165–87
[20] Alrebh A and Meunier J-L 2022 Boron nitride nanosheets synthesis in thermal plasma: an experimental and modelling analysis Plasma Chem. Plasma Process. 42 855–84
[21] Wang S et al 2023 Improving the composition and multifunctional properties of amorphous boron nitride films prepared by post-annealing assisted femtosecond pulsed laser deposition method Ceram. Int. 49 29887–96
[22] Wang H et al 2019 Scalable exfoliation and dispersion of few-layer hexagonal boron nitride nanosheets in NMP-salt solutions Appl. Surf. Sci. 488 656–61
[23] Nie X, Li G, Jiang Z, Li W, Ouyang T and Wang J 2020 Co-solvent exfoliation of hexagonal boron nitride: effect of raw bulk boron nitride size and co-solvent composition Nanomaterials 10 1035 https://mdpi.com/2079-4991/10/6/1035
[24] Morishita T, Okamoto H, Katagiri Y, Matsushita M and Fukumori K 2015 A high-yield ionic liquid-promoted synthesis of boron nitride nanosheets by direct exfoliation Chem. Commun. 51 12068–71
[25] Zhi C, Bando Y, Tang C, Kuwahara H and Golberg D 2009 Large-scale fabrication of boron nitride nanosheets and their utilization in polymeric composites with improved thermal and mechanical properties Adv. Mater. 21 2889–93
[26] Lin Y, Williams T V, Xu T-B, Cao W, Elsayed-Ali H E and Connell J W 2011 Aqueous dispersions of few-layered and monolayered hexagonal boron nitride nanosheets from sonication-assisted hydrolysis: critical role of water J. Phys. Chem. C 115 2679–85
[27] Ma Z-S, Ding H-L, Liu Z and Cheng Z-L 2019 Preparation and tribological properties of hydrothermally exfoliated ultrathin hexagonal boron nitride nanosheets (BNNSs) in mixed NaOH/KOH solution J. Alloys Compd. 784 807–15
[28] Andriani Y et al 2019 Green and efficient production of boron nitride nanosheets via oxygen doping-facilitated liquid exfoliation Ceram. Int. 45 4909–17
[29] Ali M and Abdala A 2022 Large scale synthesis of hexagonal boron nitride nanosheets and their use in thermally conductive polyethylene nanocomposites Int. J. Energy Res. 46 10143–56
[30] McKeown-Green A S et al 2024 Millimeter-scale exfoliation of hBN with tunable flake thickness for scalable encapsulation ACS Appl. Nano Mater. 7 6574–82
[31] Ge Y, Wang J, Shi Z and Yin J 2012 Gelatin-assisted fabrication of water-dispersible graphene and its inorganic analogues J. Mater. Chem. 22 17619–24
[32] Chen Y, Kang Q, Jiang P and Huang X 2021 Rapid, high-efficient and scalable exfoliation of high-quality boron nitride nanosheets and their application in lithium-sulfur batteries Nano Res. 14 2424–31
[33] Cho C-W, Pham T P T, Jeon Y-C and Yun Y-S 2008 Influence of anions on the toxic effects of ionic liquids to a phytoplankton selenastrum capricornutum Green Chem. 10 67–72
[34] Dhillon S and von Burg R 1995 Isopropyl alcohol J. Appl. Toxicol. 15 501–6
[35] Mohona T M et al 2019 Aggregation behavior of inorganic 2D nanomaterials beyond graphene: insights from molecular modeling and modified DLVO theory Environmental Science & Technology 53 4161–72
[36] Zhou K-G, Mao N-N, Wang H-X, Peng Y and Zhang H-L 2011 A mixed-solvent strategy for efficient exfoliation of inorganic graphene analogues Angew. Chem. Int. Ed. 50 10839–42
[37] Kelly A G, Vega-Mayoral V, Boland J B and Coleman J N 2019 Whiskey-phase exfoliation: exfoliation and printing of nanosheets using Irish whiskey 2D Mater. 6 045036
[38] Marsh K L, Souliman M and Kaner R B 2015 Co-solvent exfoliation and suspension of hexagonal boron nitride Chem. Commun. 51 187–90
[39] Shen J et al 2015 Liquid phase exfoliation of two-dimensional materials by directly probing and matching surface tension components Nano Lett. 15 5449–54
[40] Coleman J N et al 2011 Two-dimensional nanosheets produced by liquid exfoliation of layered materials Science 331 568–71
[41] Wang N, Yang G, Wang H, Yan C, Sun R and Wong C-P 2019 A universal method for large-yield and high-concentration exfoliation of two-dimensional hexagonal boron nitride nanosheets Mater. Today 27 33–42
[42] Vazquez G, Alvarez E and Navaza J M 1995 Surface tension of alcohol water + water from 20 to 50 .degree.C Journal of Chemical & Engineering Data 40 611–4
[43] Hugo C L, Santos M and Capelo-Martínez J-L 2009 The power of ultrasound Ultrasound in Chemistry: Analytical Applications ed J-L Capelo-Martínez (Wiley) 15
[44] Padma N 2022 Exfoliation routes to the production of nanoflakes of graphene analogous 2D materials and their applications Handbook on Synthesis Strategies for Advanced Materials: Volume-II: Processing and Functionalization of Materials ed A K Tyagi and R S Ningthoujam (Springer Nature Singapore) 377–443
[45] Gao W, Zhao Y and Yin H 2018 Lateral size selection of liquid exfoliated hexagonal boron nitride nanosheets RSC Adv. 8 5976–83
[46] Yi M, Shen Z, Liu L and Liang S 2015 Size-selected boron nitride nanosheets as oxygen-atom corrosion resistant fillers RSC Adv. 5 2983–7
[47] Liu B et al 2021 Synergistic effect of metal cations and visible light on 2D MoS2 nanosheet aggregation Environmental Science & Technology 55 16379–89

[48] Sengupta S *et al* 2024 Colloidal stabilization of hydrophobic InSe 2D nanosheets in a model environmental aqueous solution and their impact on Shewanella oneidensis MR-1 *Environmental Science: Nano* **11** 627–36
[49] Wang X *et al* 2015 Differences in the toxicological potential of 2D versus aggregated molybdenum disulfide in the lung (in eng)*Small* **11** 5079–87
[50] Wang Y, Mortimer M, Chang C H and Holden P A 2018 Alginic acid-aided dispersion of carbon nanotubes, graphene, and boron nitride nanomaterials for microbial toxicity testing *Nanomaterials* **8** 76 https://mdpi.com/2079-4991/8/2/76
[51] Cortes-Arriagada D, Barria N, Ortega D E, Araya-Duran I and Camarada M B 2022 A first-principles study on the adsorption properties of phosphorene oxide for pollutant removal from water *J. Mol. Liq.* **357** 119103
[52] Luo J M *et al* 2019 Phase-mediated heavy metal adsorption from aqueous solutions using two-dimensional layered MoS2 *ACS Appl. Mater. Interfaces* **11** 38789–97
[53] Othman Z, Mackey H R and Mahmoud K A 2022 'A critical overview of MXenes adsorption behavior toward heavy metals ' *(in English), Chemosphere* **295** 18
[54] Wang J *et al* 2020 Comparative study on the adsorption capacities of the three black phosphorus-based materials for methylene blue in water *Sustainability* **12** 8335 https://mdpi.com/2071-1050/12/20/8335
[55] Zhao L *et al* 2020 Aqueous-phase exfoliation and functionalization of boron nitride nanosheets using tannic acid for thermal management applications *Ind. Eng. Chem. Res.* **59** 16273–82
[56] Hegedűs T, Takács D, Vásárhelyi L, Szilágyi I and Kónya Z 2021 Specific ion effects on aggregation and charging properties of boron nitride nanospheres *Langmuir* **37** 2466–75
[57] Vásárhelyi L, Hegedűs T, Sáringer S, Ballai G, Szilágyi I and Kónya Z 2021 Stability of boron nitride nanosphere dispersions in the presence of polyelectrolytes *Langmuir* **37** 5399–407
[58] USEPA 2002 *Methods for measuring the acute toxicity of effluents and receiving waters to freshwater and marine organisms (EPA-821-R02-012)*
[59] Chen W *et al* 2023 Renal clearance of graphene oxide: glomerular filtration or tubular secretion and selective kidney injury association with its lateral dimension *Journal of Nanobiotechnology* **21** 51
[60] Shaybanizadeh S, Najafi Chermahini A and Luque R 2022 Boron nitride nanosheets supported highly homogeneous bimetallic AuPd alloy nanoparticles catalyst for hydrogen production from formic acid *Nanotechnology* **33** 275601
[61] Sun T *et al* 2020 Graphene plasmonic nanoresonators/graphene heterostructures for efficient room-temperature infrared photodetection *J. Semiconduct.* **41** 072907
[62] Aich N, Flora J R and Saleh N B 2012 Preparation and characterization of stable aqueous higher-order fullerenes (in eng) *Nanotechnology* **23** 055705
[63] Gorbachev R V *et al* 2011 Hunting for monolayer boron nitride: optical and Raman signatures (in eng) *Small* **7** 465–8
[64] Ali M A *et al* 2024 Influence of water chemistry and operating parameters on PFOS/PFOA removal using rGO-nZVI nanohybrid *J. Hazard. Mater.* **469** 133912
[65] Mehrabi N, Lin H and Aich N 2021 Deep eutectic solvent functionalized graphene oxide nanofiltration membranes with superior water permeance and dye desalination performance *Chem. Eng. J.* **412** 128577
[66] Lee T-W and Chen C 2024 Influence of inorganic anions on the chemical stability of molybdenum disulfide nanosheets in the aqueous environment *Environmental Science & Technology* **58** 2490–501
[67] Du M, Wu Y and Hao X 2013 A facile chemical exfoliation method to obtain large size boron nitride nanosheets *Cryst. Eng. Comm.* **15** 1782–6
[68] Jeong H *et al* 2019 Wafer-scale and selective-area growth of high-quality hexagonal boron nitride on Ni(111) by metal-organic chemical vapor deposition *Sci. Rep.* **9** 5736
[69] Li L, Chen Y, Behan G, Zhang H, Petravic M and Glushenkov A 2011 Large-scale mechanical peeling of boron nitride nanosheets by low-energy ball milling *J. Mater. Chem.* **21** 11862–6
[70] Zhang B *et al* 2017 High-efficient liquid exfoliation of boron nitride nanosheets using aqueous solution of alkanolamine (in eng) *Nanoscale Res. Lett.* **12** 596
[71] Joseph A M, Nagendra B, Bhoje Gowd E and Surendran K P 2016 Screen-printable electronic ink of ultrathin boron nitride nanosheets *ACS Omega* **1** 1220–8
[72] Mu J *et al* 2023 Thickness-dependent ultrafast nonlinear optical response of germanium selenide nanosheets *J. Mater. Sci.* **58** 11527–38
[73] Xu D *et al* 2020 Controllable nonlinear optical properties of different-sized iron phosphorus trichalcogenide (FePS3) nanosheets *Nanophotonics* **9** 4555–64
[74] Hu C-X *et al* 2022 Effects of lateral size, thickness, and stabilizer concentration on the cytotoxicity of defect-free graphene nanosheets: implications for biological applications *ACS Appl. Nano Mater.* **5** 12626–36
[75] Chen C, Shao C and Wang A 2023 Chemical exfoliating of boron nitride into edge-hydroxylated nanosheets *J. Mater. Sci.* **58** 4416–27
[76] Liu Q *et al* 2018 Porous hexagonal boron nitride sheets: effect of hydroxyl and secondary amino groups on photocatalytic hydrogen evolution *ACS Appl. Nano Mater.* **1** 4566–75
[77] Han W *et al* 2017 Water-dispersible boron nitride nanospheres with high thermal conductivity for heat-transfer nanofluids *Eur. J. Inorg. Chem.* **2017** 5466–74
[78] Wu X, Sivakumar M, Lim S S, Wu T and Heng P C 2024 Ultrasonic liquid exfoliation for producing graphene materials from rice stem: investigating cellular components and functionalities (in eng)*Ultrason. Sonochem.* **103** 106782
[79] Wang B *et al* 2024 Surface hydrophobicity of boron nitride promotes PFOA photocatalytic degradation *Chem. Eng. J.* **483** 149134
[80] Sharma K, Sharma S, Khaniya Sharma A, Paudel B, Kalita G and Tanemura M 2017 Edge controlled growth of hexagonal boron nitride crystals on copper foil by atmospheric pressure chemical vapor deposition *Cryst. Eng. Comm.* **20** 550–55
[81] Tian R *et al* 2022 Efficient exfoliation and functionalization of hexagonal boron nitride using recyclable ionic liquid crystal for thermal management applications *Chem. Eng. J.* **446** 137255
[82] Yuan F *et al* 2017 Scalable exfoliation for large-size boron nitride nanosheets by low temperature thermal expansion-assisted ultrasonic exfoliation *J. Mater. Chem.* C **5** 6359–68
[83] Li X F *et al* 2007 Synthesis and characterization of nanocrystalline hexagonal boron carbo-nitride under high temperature and high pressure *J. Phys. Condens. Matter* **19** 425235
[84] Qu J, Li Q, Luo C, Cheng J and Hou X 2018 Characterization of flake boron nitride prepared from the low temperature combustion synthesized precursor and its application for dye adsorption *Coatings* **8** 214
[85] Xiao F *et al* 2015 Edge-hydroxylated boron nitride nanosheets as an effective additive to improve the thermal response of hydrogels *Adv. Mater.* **27** 7196–203

[86] Kaur G et al 2016 Nanostructured boron nitride with high water dispersibility for boron neutron capture therapy *Sci. Rep.* **6** 1–10
[87] Sainsbury T et al 2012 Oxygen radical functionalization of boron nitride nanosheets *J. Am. Chem. Soc.* **134** 18758–71
[88] Wang Y et al 2021 Carbon-doped boron nitride nanosheets with adjustable band structure for efficient photocatalytic U(VI) reduction under visible light *Chem. Eng. J.* **410** 128280
[89] Ma X, Liu L, Zhang X and Lv T 2019 Thermal conductivity enhancement of polyimide films filled with BN and AlN fillers *High Perform. Polym.* **31** 959–68
[90] Pilli A, Jones J, Chugh N, Kelber J, Pasquale F and LaVoie A 2019 Atomic layer deposition of BN as a novel capping barrier for B_2O_3 *Journal of Vacuum Science & Technology* A **37** 1–12
[91] Kaszuba M, Corbett J, Watson F M and Jones A 2010 High-concentration zeta potential measurements using light-scattering techniques *Philosophical Transactions of the Royal Society A: Mathematical, Physical and Engineering Sciences* **368** 4439–51
[92] Li J et al 2018 Boron nitride nanosheets reinforced waterborne polyurethane coatings for improving corrosion resistance and antifriction properties *Eur. Polym. J.* **104** 57–63
[93] Wang Z, Zhu Y, Ji D, Li Z and Yu H 2020 Scalable exfoliation and high-efficiency separation membrane of boron nitride nanosheets, *Chemistry Select* **5** 3567–73
[94] Li Z et al 2023 Hydroxyl boron nitrid e/natural rubber composites with enhanced mechanical and thermal conduction properties: implications for heat dissipative tires or conveyor belts *ACS Appl. Nano Mater.* **6** 5365–73
[95] Das S K, Bedar A, Kannan A and Jasuja K 2015 Aqueous dispersions of few-layer-thick chemically modified magnesium diboride nanosheets by ultrasonication assisted exfoliation *Sci. Rep.* **5** 10522
[96] Ren J, Stagi L and Innocenzi P 2021 Hydroxylated boron nitride materials: from structures to functional applications *J. Mater. Sci.* **56** 4053–79
[97] Castillo A M, Sharpe D M T, Ghalambor C K and De León L F 2018 Exploring the effects of salinization on trophic diversity in freshwater ecosystems: a quantitative review *Hydrobiologia* **807** 1–17
[98] Höss S, Rauchschwalbe M-T, Fueser H and Traunspurger W 2022 Food availability is crucial for effects of 1-μm polystyrene beads on the nematode Caenorhabditis elegans in freshwater sediments *Chemosphere* **298** 134101
[99] Zou W, Huo Y, Zhang X, Jin C, Li X and Cao Z 2024 Toxicity of hexagonal boron nitride nanosheets to freshwater algae: phospholipid membrane damage and carbon assimilation inhibition *J. Hazard. Mater.* **465** 133204
[100] Wang N et al 2017 Toxicity evaluation of boron nitride nanospheres and water-soluble boron nitride in Caenorhabditis elegans *Int. J. Nanomedicine* **12** 5941–57